Advanced Powder Materials 3 (2024) 100243

Contents lists available at ScienceDirect

Advanced Powder Materials

journal homepage: www.keaipublishing.com/en/journals/advanced-powder-materials

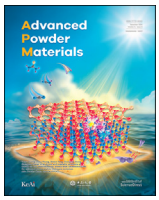

Atmosphere engineering of metal-free Te/C_3N_4 p-n heterojunction for nearly 100% photocatalytic converting CO_2 to CO

Huange Liao [a], Kai Huang [b], Weidong Hou [a], Huazhang Guo [a], Cheng Lian [b], Jiye Zhang [c], Zheng Liu [d,*], Liang Wang [a,**]

[a] Institute of Nanochemistry and Nanobiology, School of Environmental and Chemical Engineering, Shanghai University, Shanghai 200444, China
[b] State Key Laboratory of Chemical Engineering, Shanghai Engineering Research Center of Hierarchical Nanomaterials, and School of Chemistry and Molecular Engineering, East China University of Science and Technology, Shanghai 200237, China
[c] School of Materials Science and Engineering, Shanghai University, Shanghai 200444, China
[d] School of Materials Science and Engineering, Nanyang Technological University, 50 Nanyang Avenue, 639798, Singapore

ARTICLE INFO

Keywords:
p-n heterojunction
Carbon nitride
Built-in electric field
Photocatalytic carbon dioxide reduction
Heterojunction photocatalysts

ABSTRACT

Carbon nitride (CN)-based heterojunction photocatalysts hold promise for efficient carbon dioxide (CO_2) reduction. However, suboptimal production yields and limited selectivity in CO_2 conversion pose significant barriers to achieving efficient CO_2 conversion. Here, we present the construction of a p-n heterojunction between ultrasmall Te NPs and CN nanosheet using a novel tandem hydrothermal-calcination synthesis strategy. Through ammonia-assisted calcination, ultrasmall Te NPs are grown in-situ on the CN nanosheets' surface, resulting in the generation of a robust p-n heterojunction. The synthesized heterojunction exhibits increased specific surface area, reinforced visible light absorption, intensive CO_2 adsorption capacity, and efficient charge transfer. The optimum Te/CN-NH_3 demonstrates superior photocatalytic CO_2 reduction activity and durability, with nearly 100 % selectivity for CO and a yield as high as 92.0 μmol g^{-1} h^{-1}, a fourfold increase compared to pure CN. Experimental and theoretical calculations unravel that the strong built-in electric field of the Te/CN-NH_3 p-n heterojunction accelerates the migration of photogenerated electrons from Te NPs to the N site on CN nanosheets, thereby promoting CO_2 reduction. This study provides a promising material design approach for the construction of high-performance p-n heterojunction photocatalysts.

1. Introduction

Solar-driven carbon dioxide (CO_2) reduction has emerged as a pivotal strategy for converting CO_2 into high-value-added chemicals and fuels, addressing current global environmental and climate challenges [1–3]. Among the myriad photocatalysts investigated for this purpose, graphitic carbon nitride (CN) has garnered significant attention as a metal-free n-type organic semiconductor [4,5]. Its appeal lies in its responsiveness to visible light, remarkable chemical stability, intriguing electronic structure, environmental friendliness, and economic viability [6]. Nevertheless, the intrinsic limitations of pure CN photocatalysts, including inefficient separation of photogenerated carriers and a relatively small specific surface area, impede their full potential in CO_2 photoreduction [7,8]. Therefore, it is deep desirability to develop innovative strategies to surmount these bottlenecks.

In recent years, the exploration of CN-based heterojunctions has gained significant momentum, propelled by the pursuit of enhancing carrier separation efficiency and optimizing photocatalytic performance [9,10]. Among the various types of explored heterojunction architectures, the CN-based p-n heterojunction has emerged as a prominent candidate, distinguished by its inherent built-in electric field [11]. This attribute facilitates expedited charge transfer dynamics and mitigates the ultrafast electron-hole recombination phenomena observed on semiconductor surfaces [12], such as Cu_2O/CN [13], Co_3O_4/CN [14], $CoWO_4$/CN [15], $CoFe_2O_4$/CN [16], BiOI/CN [17], displaying excellent performance in the photocatalytic field. Nevertheless, despite these significant strides, extant CN-based p-n heterojunctions encounter challenges such as suboptimal production yields and limited production selectivity in CO_2 photoconverted progress, thereby posing a huge barrier to achieving efficient CO_2 conversion [18,19]. Tellurium (Te),

* Corresponding author.
** Corresponding author.
E-mail addresses: Z.Liu@ntu.edu.sg (Z. Liu), wangl@shu.edu.cn (L. Wang).

https://doi.org/10.1016/j.apmate.2024.100243
Received 3 July 2024; Received in revised form 3 September 2024; Accepted 18 September 2024
Available online 26 September 2024

recognized as a typical p-type semiconductor, demonstrates exceptional characteristics including rapid photoelectric response, pronounced light absorption, and notable carrier mobility, rendering it highly coveted across various applications [20,21]. In addition, Te exhibits remarkable CO_2 adsorption capabilities, rendering it particularly promising for integration into CO_2 reduction processes [22]. Therefore, there exists a compelling impetus to harness the synergistic interplay between Te and CN to engineer p-n heterojunctions aimed at addressing the current issues and maximizing their advantages in the domain of CO_2 reduction.

Herein, we present a novel tandem hydrothermal-calcination synthesis strategy for the fabrication of a p-n heterojunction between ultrasmall Te nanoparticles (NPs) and CN nanosheet, achieved through simple atmosphere modulation. Following ammonia-assisted calcination, ultrasmall Te NPs were grown in-situ on the CN nanosheets' surface, resulting in the construction of a robust p-n heterojunction. The synthesized heterojunction exhibited enhanced visible light absorption, intensive CO_2 adsorption capacity, and efficient charge separation, culminating in nearly 100 % selectivity for CO products in a gas-solid phase test system for photocatalytic CO_2 reduction, with impressive yields of up to 92.0 μmol g^{-1} h^{-1}. The elucidation of the mechanism underlying directed interfacial charge transfer in the p-n heterojunction was facilitated through advanced characterization techniques, including Kelvin probe microscopy (KPFM) and electrostatic force microscopy (EFM). Furthermore, the dynamic behavior of the photocatalytic CO_2 reduction process was identified using in-situ diffuse reflectance infrared Fourier transform spectroscopy (DRITFs). To provide deeper insights into the underlying mechanisms, density-functional theory (DFT) calculations were performed to further corroborating the experimental findings. Our study unveils a promising avenue for the synthesis of high-performance p-n heterojunctions, thus laying the groundwork for the development of innovative materials for sustainable energy applications.

2. Results and discussion

2.1. Construction of Te/CN p-n heterojunction and characterization of morphology and structure

The synthesis of Te/CN p-n heterojunctions was accomplished using a novel tandem hydrothermal-calcination strategy under NH_3 atmosphere, as shown in Fig. 1a. Initially, telluric acid was introduced into a melamine matrix to form a supramolecular intermediate precursor during a hydrothermal reaction. The resultant intermediate precursor exhibited a hexagonal prism morphology (Fig. S1) [23], and its XRD pattern (Fig. S2) aligns closely with previously reported data. Subsequently, high calcination temperature was employed to induce the transformation of the intermediate precursors in an NH_3/N_2 environment, facilitating the in-situ growth of ultrasmall Te NPs on CN nanosheets, labelled as Te/CN-NH_3. During the high-temperature calcination process, the CN intermediates initially transform from rods into tubes. As the reaction progresses, these tubes further disintegrate into nanosheets, while telluric acid molecules continuously aggregate into Te NPs and grow on the CN nanosheets. Concurrently, NH_3 decomposes at 500 °C, resulting in

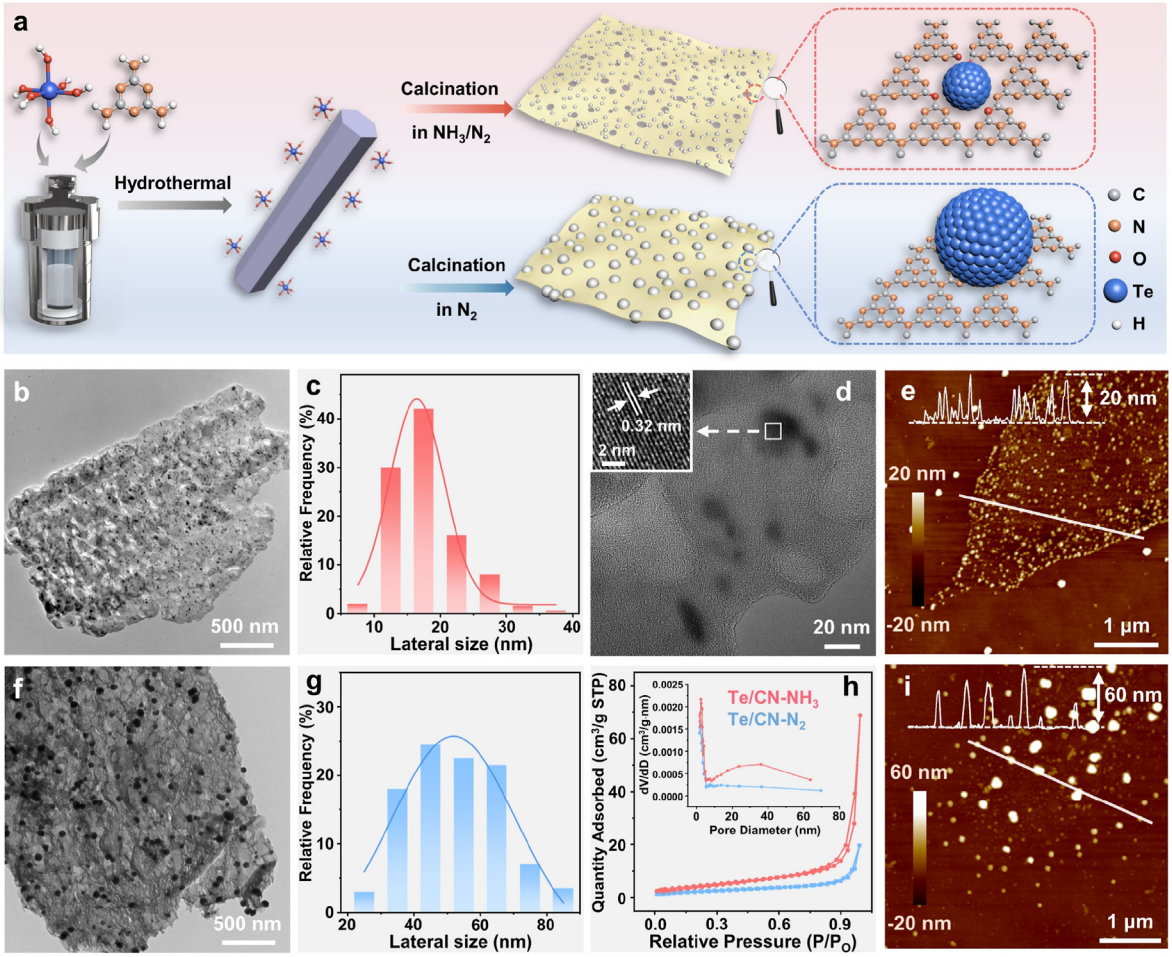

Fig. 1. (a) Schematic preparation process of Te/CN p-n heterojunction; (b–e) The TEM (b), particle size distribution (c), HRTEM (d), and AFM (e) images of Te/CN-NH_3; (f–g) The TEM (f) and particle size distribution (g) of Te/CN-N_2; (h) N_2 adsorption-desorption isotherms and corresponding pore size distribution profiles (the inset) of samples; (i) The AFM image of Te/CN-N_2.

the formation of micropores within the CN substrates, which in turn provide additional reactive sites [24]. Moreover, NH_3 played a pivotal role in the incorporation of N atoms into CN substrate, thereby facilitating the trapping of Te NPs within the microporous sites. For comparative analysis, Te/CN-N_2 was also prepared under an N_2 atmosphere.

The morphology and microstructure of the synthesized photocatalysts were observed using transmission electron microscopy (TEM). TEM images revealed the characteristic two-dimensional (2D) sheet-like morphology of pure CN (Fig. S3), while Te NPs were uniformly dispersed on CN nanosheets without noticeable agglomeration (Fig. 1b–f). Notably, the Te/CN-NH_3 composite presented a morphology characterized by CN nanosheets loaded with Te NPs, with the transparent spots indicating a porous feature. Meanwhile, the SEM image of the Te/CN-NH_3 composite reveals that the Te NPs are embedded within the CN nanosheets as opposed to being merely adhered onto their surface (Fig. S4). This configuration facilitates the formation of heterojunctions characterized by direct surface contact between the Te NPs and the CN nanosheets. Furthermore, the average size of Te NPs exhibited significant variation between samples calcined under different atmospheres. Particle size distribution analysis revealed that Te NPs calcined in an NH_3/N_2 atmosphere possessed an average size of about 18 nm (Fig. 1c), considerably smaller than those calcined under N_2 atmosphere, which exhibited an average size of about 52 nm (Fig. 1g). This observation suggests that the presence of NH_3 inhibited the excessive growth of Te NPs during the calcination process. High-resolution TEM (HRTEM) analysis provided further insights into the porous nature of Te/CN-NH_3 with mesopore diameters ranging from 20 to 40 nm, attributed to the Te sublimation-induced porogenesis. This porous structure affords abundant active sites for immobilizing CO_2 molecules. Besides, the synthesized CN nanosheets are amorphous, and the obvious lattice stripes observed on Te/CN-NH_3 belong to Te NPs with a spacing of 0.32 nm (Fig. 1d), corresponding to the (101) plane of Te [20]. The homogeneous distribution of C, N, O, and Te elements throughout the Te/CN-NH_3 structure was detected using Energy dispersive X-ray (EDX) mapping (Fig. S5), further substantiating the successful integration of Te NPs with CN nanosheets.

Brunauer–Emmett–Teller (BET) specific surface area and corresponding pore size distribution profiles were evaluated through nitrogen adsorption–desorption isotherms to explore the influence of the calcination atmosphere on the catalysts. As shown in Fig. 1h and Table S1, both Te/CN-NH_3 and Te/CN-N_2 exhibited typical type IV isotherms and type H3 hysteresis [25]. The specific BET surface area of the samples increased from 8.97 $m^2\ g^{-1}$ (Te/CN-N_2) to 16.42 $m^2\ g^{-1}$ (Te/CN-NH_3), attributed to the porogenesis induced by the NH_3 atmosphere. Pore size distribution analysis demonstrated that Te/CN-NH_3 exhibited a mesopore structure with mesopore size distribution at 25.91 nm, larger than that of Te/CN-N_2 (13.54 nm). Te/CN-NH_3 exhibits a larger surface area and more pores compared to Te/CN-N_2, indicating that pyrolysis in an

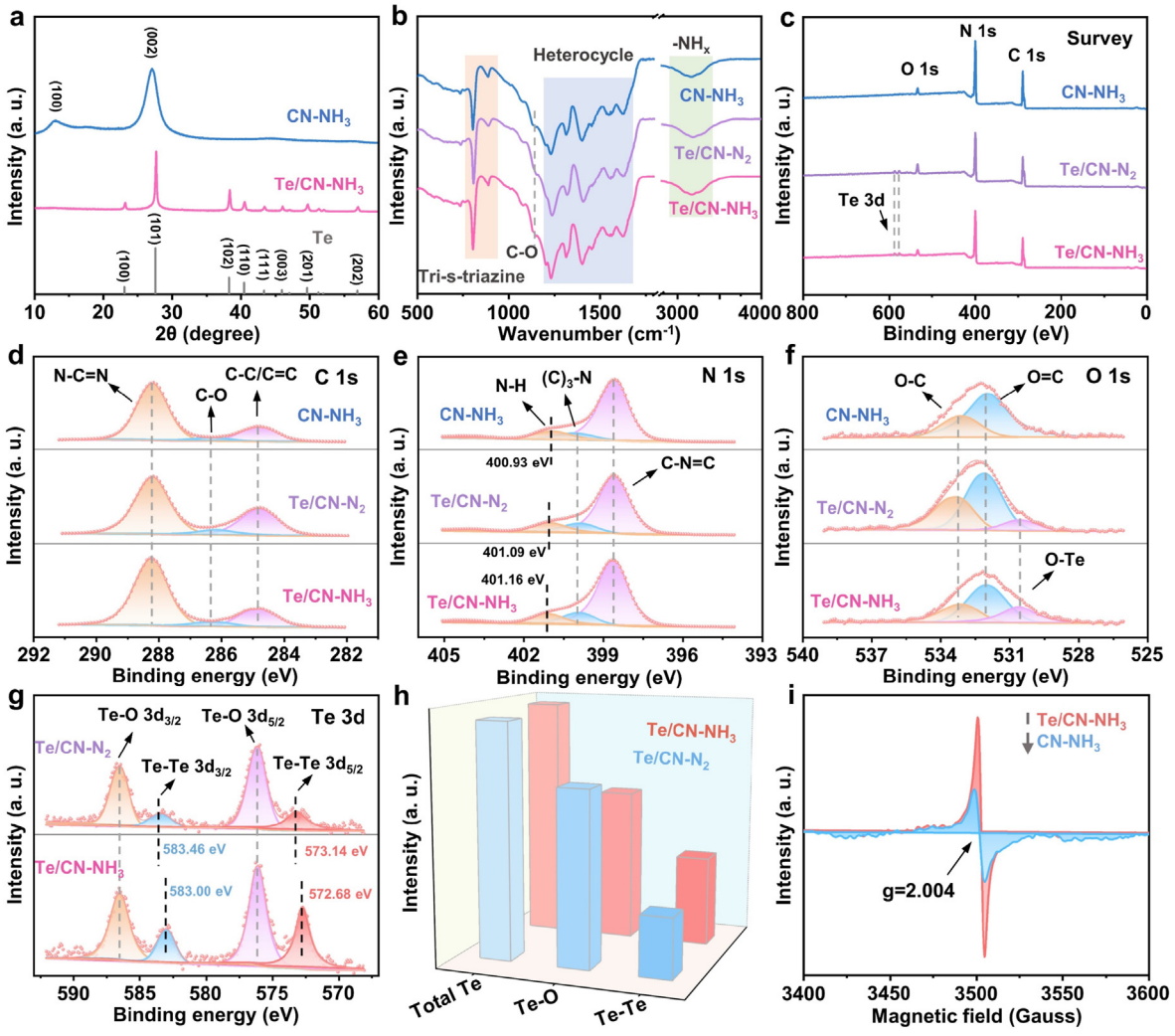

Fig. 2. (a) The XRD spectra of CN-NH_3, Te/CN-NH_3, and PDF standard card of Te; (b) The FT-IR spectra of CN-NH_3, Te/CN-N_2, and Te/CN-NH_3; (c–g) The XPS Survey (c), XPS C 1s (d), XPS N 1s (e), XPS O 1s (f), and XPS Te 3d (g) spectra of CN-NH_3, Te/CN-N_2 and Te/CN-NH_3; (h) The amount of different Te in Te/CN-N_2 and Te/CN-NH_3 based on the XPS Te 3d spectra; (i) The EPR spectra of CN-NH_3 and Te/CN-NH_3.

NH_3 atmosphere were conducive to form substantial mesoporous and exposed increased numbers of active sites [26]. Furthermore, atomic force microscope (AFM) images illustrated that the height of Te/CN-NH_3 (Fig. 1e) was lower than that of Te/CN-N_2 (Fig. 1i), with Te NPs evenly distributed on the CN nanosheets, consistent with TEM results. This observation reveals that the NH_3 atmosphere suppressed the stacking between CN layers, forming the ultra-thin CN structure during the calcination process. Thus, the unique Te NPs anchored on the surface of CN nanosheets might modulate the electronic structure of active centers and optimize catalytic behavior.

X-ray diffraction (XRD) patterns exhibit the crystal structure of the samples (Fig. 2a). The diffraction pattern of CN-NH_3 displays two evident peaks at 12.9° and 27.2°, corresponding to the (100) and (002) crystal planes of CN, originating from the intra-planar stacking of the tris-s-triazine cells and the interfacial stacking of conjugated aryl groups, respectively [27]. The diffraction peaks of Te/CN-NH_3 corresponds to the standard card of Te, further affirming the successful synthesis of the Te/CN heterojunction [28]. However, the two diffraction peaks of CN were not clearly discernible due to their weak intensity relative to the diffraction peaks of Te. The lattice fringe of Te/CN-NH_3 was estimated to be 0.32 nm, consistent with HRTEM results.

Fourier transform infrared spectroscopy (FT-IR) and high-resolution X-ray photoelectron spectroscopy (XPS) was employed to elucidate the elemental composition and chemical state of as-prepared catalysts. As depicted in Fig. 2b, CN-NH_3, Te/CN-N_2, and Te/CN-NH_3 exhibited similar infrared spectra, featuring prominent absorptions at 810, 1200–1600, and 3000-3300 cm^{-1}, corresponding to the tri-s-triazine unit respiration vibration, stretching vibration of C-N heterocyclic ring, and stretching vibration of N-H, respectively [29]. Additionally, a weaker absorption at 1150 cm^{-1} corresponds to the stretching vibration of C-O. The XPS survey spectra confirmed the existent of the elements C, N, and O in CN-NH_3 (Fig. 2c) and CN-N_2 (Fig. S6), with the presence of Te detected in the composites, affirming the combination of Te with CN successfully. Moreover, the N contents of the prepared samples were identified to be 45.08, 50.65, 50.52 and 51.94at.% for Te/CN-N_2, Te/CN-NH_3, CN-N_2, and CN-NH_3, respectively. The increasing contents of edge-type N could be attributed to the NH_3-assisted synthesis effects, facilitating the anchoring of small Te NPs at mesoporous edges due to sufficient anchoring sites for immobilizing Te NPs. Further insight is provided by the high-resolution spectra of C 1s, N 1s, O 1s and Te 3d (Fig. 2d–g). The high-resolution C 1s spectra exhibits peaks centered at 284.8 eV (C–C/C=C) and 288.2 eV (N–C=N), originating from the framework of the CN [30]. The high-resolution N 1s spectra could be deconvoluted into three peaks at 398.6, 399.9, and 400.93 eV, assigned to C–N=C, $(C)_3$-N, and N-H of the CN, respectively [31]. Notably, the introduction of Te NPs causes the N-H bonds to shift slightly towards higher binding energy, indicating a reduction in electron cloud density around the nitrogen atoms in CN due to the close interaction with Te NPs. This shift confirms the successful formation of a p-n heterojunction. Specifically, Te/CN-N_2 exhibits a positive shift of 0.16 eV, whereas Te/CN-NH_3 shows a more pronounced positive shift of 0.23 eV. This larger shift suggests that the heterojunction calcined in NH_3 is more robust, thereby enhancing the influence of Te NPs on the electron cloud density in CN.

The O element present in the samples derived from atmospheric oxygen and oxygen atoms in telluric acid. In addition to the observed peaks at 532.1 eV (O=C) and 533.1 eV (O–C) in the high-resolution O 1s spectra of the composites, a peak at 530.6 eV corresponding to O-Te bonds is evident [32]. The presence of O-Te bonds is attributed to the incomplete removal of oxygen from telluric acid during the calcination process, resulting in residual O-Te bonds. Additionally, Te may form bonds with oxygen atoms in the CN structure, as Te has a strong affinity for bonding with oxygen. Furthermore, the Te–O bonds are observed at 576.0 eV (Te $3d_{5/2}$) and 586.5 eV (Te $3d_{3/2}$) in the high-resolution Te 3d spectra [33]. Notably, the Te–Te bonds in Te/CN-NH_3 at 572.68 eV (Te $3d_{5/2}$) and 583.00 eV (Te $3d_{3/2}$) exhibit a negative shift of 0.46 eV compared to those in Te/CN-N_2 (573.14 eV and 583.46 eV). This phenomenon indicates that the NH_3 calcination process changes the coordination microenvironment of Te, leading to an increase in the electron cloud density surrounding the Te NPs in Te/CN-NH_3 [32,34]. Moreover, the elemental content of Te in Te/CN-NH_3 is slightly higher than that in Te/CN-N_2 (Fig. 2h and Table S2) due to the decrease in O content and increase in N content under NH_3-assisted calcination condition. This results in a decrease in Te–O bonds and an increase in Te-Te bonds on the surface of Te/CN-NH_3.

The electronic properties of the materials were characterized by electron paramagnetic resonance spectroscopy (EPR). As shown in Fig. 2i, the EPR spectrum of CN-NH_3 displays a single Lorentzian line at $g = 2.004$, caused by π-conjugated electrons formed by lone pairs of electrons on the carbon atoms of the tris-triazine ring. After the introduction of Te NPs, the EPR signals of the composites were distinctly enhanced, indicating a tight interaction between Te NPs and CN, facilitating more efficient expansion of π–π conjugated delocalization. That is, the surface electrons of Te/CN-NH_3 are more abundant than those of CN-NH_3. The higher concentration of uncoupled electrons in Te/CN-NH_3 facilitates the photo-induced generation of reactive intermediates, thus enhancing the photocatalytic activity [35].

2.2. Evaluation of CO_2RR activity

The photocatalytic activity of the catalysts was assessed in the existence of only H_2O and CO_2 gas. As depicted in Fig. 3a and Fig. S7, CO emerges as the primary product. The average CO yield of CN-N_2 is 23.0 μmol g^{-1} h^{-1}, slightly lower than that of CN-NH_3 (32.2 μmol g^{-1} h^{-1}). After introducing of Te NPs, the content of Te in the composites increased with the addition of telluric acid (Table S3), and the catalytic capability increased first and then decreased (Fig. S8), reaching its zenith when the ratio of telluric acid to melamine was 0.4:1. Meanwhile, the calcination temperature was optimized, with the superior properties observed when calcined at 500 °C. In the reduction test using high concentration CO_2, the average CO yield of Te/CN-NH_3 synthesized under optimal conditions reached 92.0 μmol g^{-1} h^{-1}, with nearly 100 % product selectivity, surpassing most reported CN-based and other p-n heterojunctions photocatalytic materials in similar testing environments (Table S4). The apparent quantum yield (AQY) of Te/CN-NH_3 stood at 0.01 % at $\lambda = 420$ nm. The highest catalytic activity of Te/CN-NH_3 indicates the advantages of the p-n heterojunction formed under NH_3 assisted calcination in facilitating prominent photoreduction.

To validate that CO was indeed generated from the CO_2 reduction reaction catalyzed by Te/CN-NH_3, a control-experiment was carried out by alternately omitting light, CO_2, and catalyst from the photocatalysis reaction [36]. The controlled experiment confirmed that no CO product was produced when any of the conditions of CO_2, light, and catalyst were not met, thereby verifying that CO and CH_4 were produced from the photoreduction of CO_2 by the catalyst. In addition, $^{13}CO_2$ isotope labeling experiments (Fig. 3b and Fig. S9) were implemented to elucidate the source of products. When utilizing $^{13}CO_2$ as the stock, mass spectroscopy revealed distinct signals for ^{13}CO (m/z=29), which demonstrates that the product originated from CO_2 rather than the decomposition of the catalyst [37]. Furthermore, Te/CN-NH_3 exhibited stable catalytic performance over four cycle experiments (Fig. 3c). To investigate the reduction ability of the catalyst at low concentrations of CO_2, high purity CO_2 was diluted with N_2 to decrease the concentration, and the photoreduction test was carried out at different CO_2 concentrations [38]. Te/CN-NH_3 demonstrated good photoreduction performance even at low concentrations of CO_2 and in air (Fig. 3d).

The adsorption properties of Te/CN-NH_3 on the reaction substrate were investigated using CO_2-temperature programmed desorption (CO_2-TPD, Fig. 3e**)** and water contact angle measurement (Fig. S10). The results revealed that samples subjected to NH_3-assisted calcination exhibited stronger CO_2-TPD signals compared to those calcined in N_2, indicating that NH_3-assisted calcination enhanced the abundance of

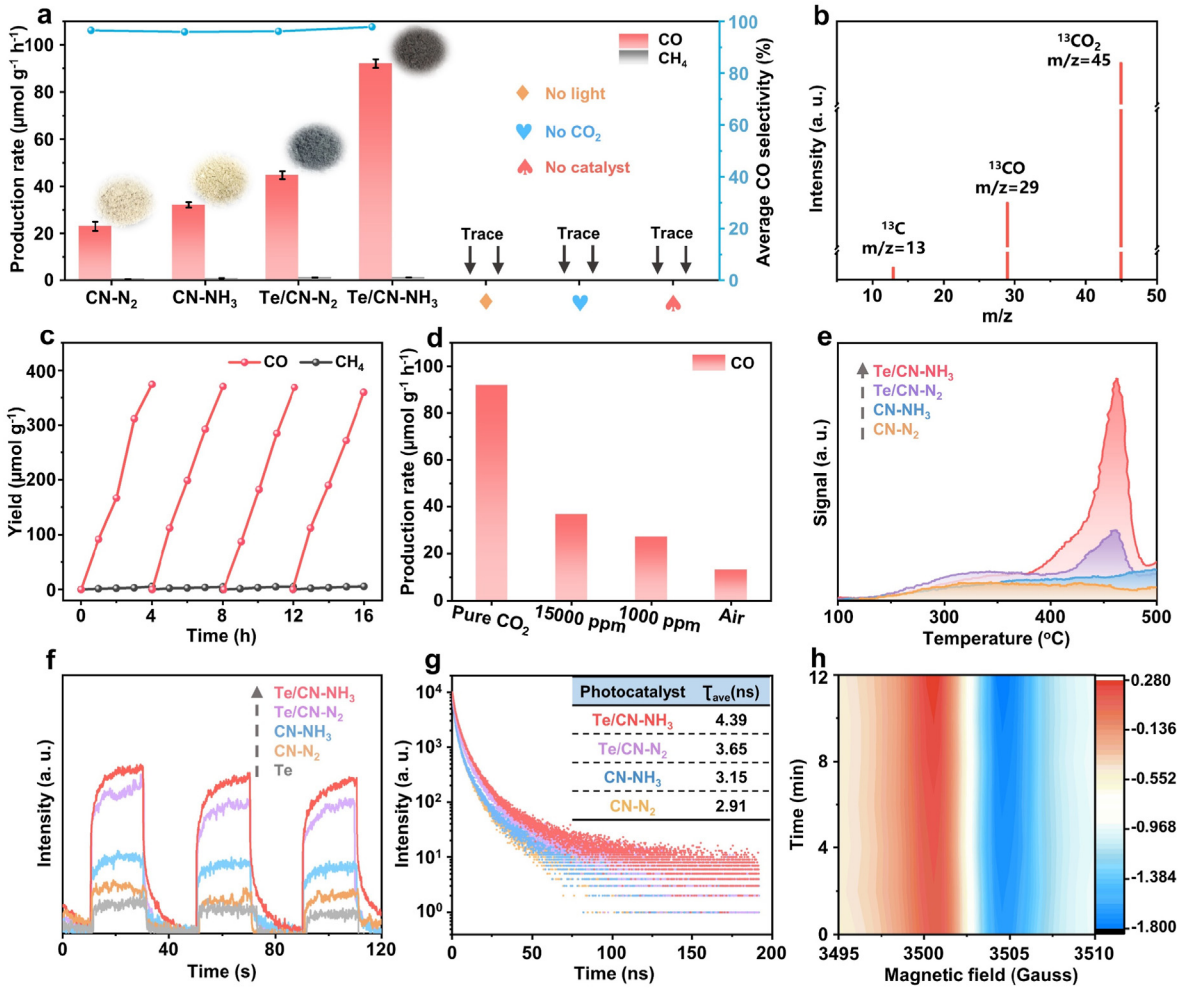

Fig. 3. (a) The photoreduction activities of the synthesized samples and control experiments in pure CO_2; (b) Mass spectrum of the products from the $^{13}CO_2$ photoreduction by Te/CN-NH_3; (c) Cycling experiments of CO_2RR in pure CO_2 of Te/CN-NH_3; (d) The photoreduction activities of Te/CN-NH_3 under different concentrations of CO_2; (e) CO_2-TPD profiles of the samples; (f) The photocurrent curves of the samples; (g) The time-resolved transient fluorescence spectra of the samples; (h) The *in-situ* EPR spectrum of Te/CN-NH_3.

alkaline sites on the sample surface [39,40]. Additionally, the introduction of Te NPs led to a significant enhancement in the CO_2-TPD signal due to strong CO_2 adsorption capabilities of Te. Te/CN-N_2 exhibits two CO_2-TPD signals located at 330 and 460 °C. Upon changing the synthesis atmosphere from N_2 to NH_3, Te/CN-NH_3 display a stronger intensity of CO_2-TPD signal peak at 460 °C compared to Te/CN-N_2, showing more effective chemisorption of CO_2. The water contact angle of Te/CN-NH_3 is about 21°, indicating good wettability [41]. Therefore, the synergistic effect of good hydrophilicity and excellent CO_2 chemical absorbability facilitates the robust CO_2 photoreduction activity of Te/CN-NH_3.

The transient photocurrent curve (I-t, Fig. 3f) evidences that the composite exhibits a higher photocurrent compared to pure CN, indicating superior charge separation efficiency [42]. NH_3-assisted calcination enhanced the photocurrent of the samples relative to those calcined under N_2 atmosphere, with Te/CN-NH_3 exhibiting the highest photocurrent density [43]. This highlighted the advantageous effect of NH_3-assisted calcination on charge transfer within the heterojunction. Electrochemical impedance spectroscopy (EIS, Fig. S11) corroborates this observation. The minimum Nyquist radius of Te/CN-NH_3 indicates the least charge transfer resistance, and high-efficiency charge transfer between Te and CN [44,45]. In addition, the photoluminescence (PL, Fig. S12) spectra verified the effective charge separation of the sample. The weaker fluorescence intensity of Te/CN-NH_3 and Te/CN-N_2 compared to CN indicates that heterojunction formation effectively inhibits carrier recombination [46]. Particularly noteworthy is that the fluorescence of Te/CN-NH_3 is weaker than that of Te/CN-N_2, suggesting that the NH_3-assisted calcination strategy provides an effective non-radiative decay pathway for the photogenerated carrier between Te and CN. The dynamic behavior of photo-induced carriers was further investigated by time-resolved transient fluorescence (Fig. 3g) spectroscopy. The results show that Te/CN-NH_3 exhibits the longest fluorescence lifetime, signifying the strongest charge separation [47]. *In-situ* EPR (Fig. 3h) was employed to analyze the charge density changes of Te/CN-NH_3 heterojunction after illumination. The EPR signal of Te/CN-NH_3 gradually increased with illumination, reaching stability at 10 min. This suggests that strong electron-hole pair separation occurs in the catalyst after photoexcitation, resulting in the gradual accumulation of unpaired electron concentration, which then maintained a dynamic equilibrium after reaching the maximum value [48]. These summaries consistently affirm that Te/CN-NH_3 demonstrates robust carrier separation capacities.

2.3. *Strong built-in electric field formed by Te/CN p-n heterojunction*

To probe the charge transfer dynamics between Te NPs and CN nanosheets, we conducted an in-depth analysis of the band structure using UV–vis diffuse reflection spectroscopy (DRS) and Mott-Schottky analysis. As depicted in Fig. S13, CN manifests significant light

absorption up to 460 nm, while Te NPs exhibits pronounced absorption across the visible light spectrum. After the formation of heterojunction, the composite materials exhibit substantially enhanced light absorption compared to pure CN. According to the converted Kubelka-Munk function, we determined the bandgaps of Te NPs and CN to be 2.50 and 2.62 eV, respectively. Mott-Schottky curve (Fig. S14) was employed to determine the conduction type and flat-band potential of the samples. Notably, Te NPs is confirmed as a p-type semiconductor indicated by the negative slope, while CN exhibits properties of an n-type semiconductor, as evidenced by the positive slope. The Mott-Schottky diagram of the Te/CN composites displays an inverted "V-shape", a typical characteristic of p-n heterojunctions [49], confirming the successful construction of Te/CN p-n heterojunctions. The transverse intercept values of 0.43 eV and −0.55 eV (vs Ag/AgCl, pH=7) correspond to the flat-band potentials of Te NPs and CN, respectively. Further analysis of the band structure reveals the conduction and valence band potentials (CB/VB) of Te NPs and CN to be −1.67/0.83 eV and −0.55/2.07 eV, respectively (vs. NHE, pH=7). Notably, the CB potential of CN is more negative than that of CO_2/CO, while the VB potential of Te NPs is more positive than that of H_2O/O_2 [50]. From a thermodynamic point of view, these values verify that the synthesized sample possesses adequate redox capacity to facilitate the reduction of CO_2 to CO and CH_4, as well as the oxidation of H_2O to O_2. Furthermore, the abundant microporous structure of the samples calcined under NH_3 exposes more reactive sites. This structural feature facilitates the CO_2 reduction at the CN terminals within the heterojunction, enhancing the overall reactivity and efficiency of the process.

To further investigate the charge transfer mechanism within Te/CN heterojunction, in-situ KPFM and EFM were employed to record the surface potential of the sample and detect the local charge change. Since the interfacial charge transfer process is closely related to the work function (WF), the WF can be calculated from the surface potential measured by KPFM. As depicted in Fig. S15b, the contact potential difference (CPD) between Te NPs and the probe is measured to be 37 mV. The WF_{Te} of Te NPs is determined to be 4.74 eV using the equation WF(eV)=4.7 eV + e × CPD, where e is the electron charge and 4.7 eV is the work function of the corrected probe (SCM-PIT-V2) [51]. Similarly, the CPD_{CN} of CN is −23 mV (Fig. S15d), yielding a corresponding WF_{CN} of 4.68 eV. While the CPD_1 between Te/CN-NH_3 and the probe is 27 mV (Fig. 4a–c), it can be inferred that the WF_1 of Te/CN-NH_3 is 4.73 eV. After determining the WF, the Fermi energy level (EF) of Te/CN-NH_3 is significantly lower than that of CN, indicating that when Te NPs and CN

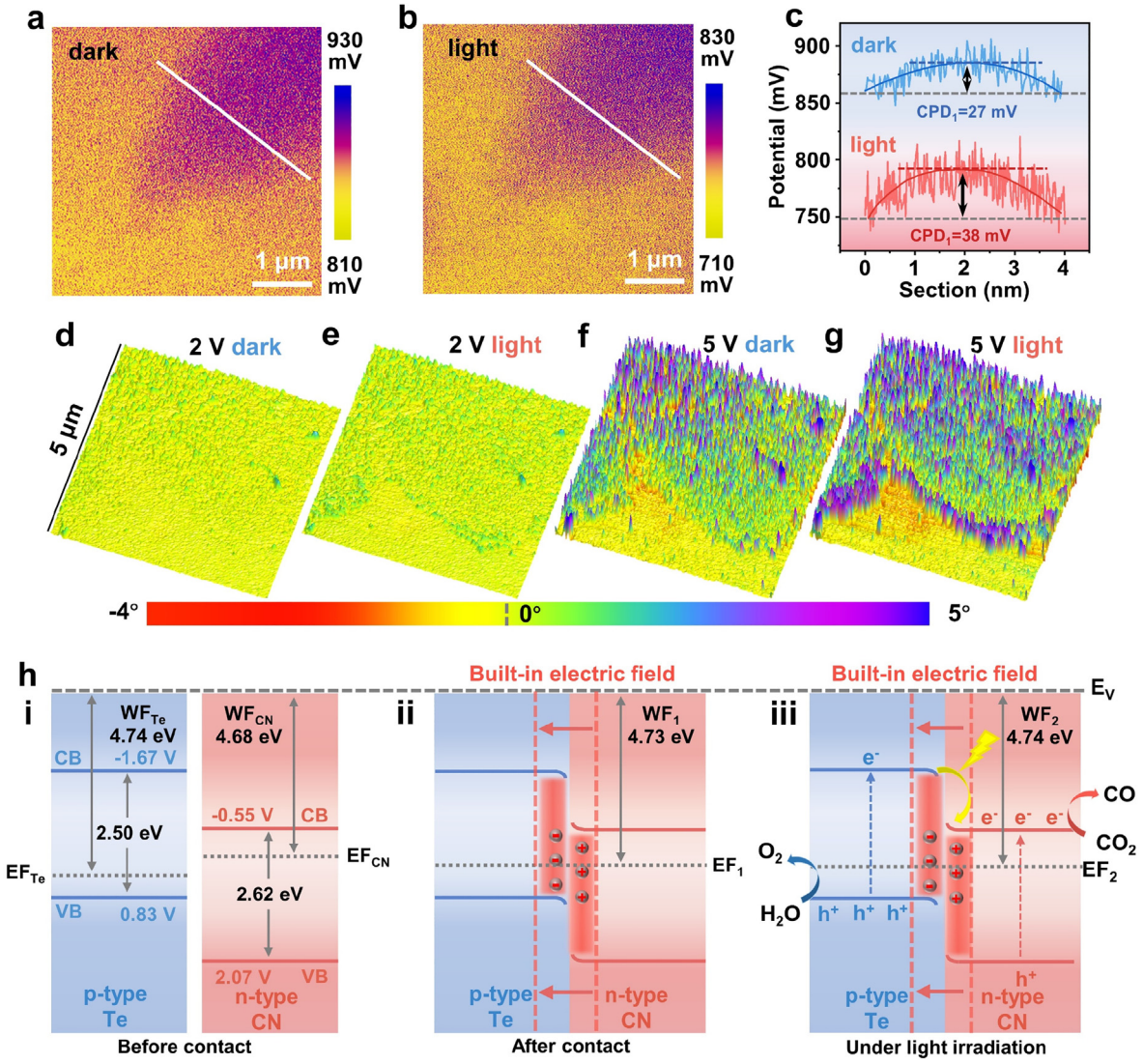

Fig. 4. (a–c) KPFM image of Te/CN-NH_3 (a) in dark, (b) under light irradiation, and (c) the corresponding liner scanning of CPD along the white lines; (d–g) 3D EFM images of Te/CN-NH_3 at sample bias of 2 V (d) in dark and (e) under light irradiation, and at sample bias of 5 V (f) in dark and (g) under light irradiation; (h) Schematic of the built-in electric field to facilitate efficient charge transfer process.

are in tight contact, electrons are spontaneously migrated from CN to Te NPs through the heterogeneous boundary [52,53]. The CPD between Te/CN-NH_3 and the probe under light irradiation (CPD_2=38 mV, Fig. 4b–c) is larger than that in the dark environment, indicating that Te NPs loses electrons under light irradiation and increases the surface potential. The built-in electric field drives photogenerated electrons from CB of Te NPs to that of CN, and photogenerated holes from VB of CN to that of Te NPs under illumination (Fig. 4h) [12]. Moreover, Te/CN-NH_3 exhibits a higher CPD to the probe than Te/CN-N_2 under both dark and light conditions (Figs. S15e–f, CPD_3=16 mV, CPD_4=20 mV), indicating that the enhanced charge transfer within the heterojunction facilitated by the NH_3-assisted calcination strategy [54,55].

To comprehensively understand the built-in electric field within the Te/CN heterojunction, it is imperative to evaluate its magnitude [56]. According to the method reported by Kanata et al. [57], the built-in electric field is mainly determined by the surface voltage (Vs) and the surface charge density (ρ), which are characterized via KPFM and transient photocurrent density measurement, respectively (Figs. S16 and S17). As shown in Fig. S18, the Te/CN-NH_3 heterostructure exhibits a notably heightened built-in electric field, exceeding that of Te/CN-N_2 by a factor of 8.4 times. This built-in electric field would significantly promote the effective separation and transfer of interface charges.

For EFM measurements, sample bias of 2 V and 5 V is applied, equivalent to negative pressure applied to the probe. In the dark environment, the surface phase change of Te NPs is positive (Fig. 4d), indicating repulsion between Te NPs and the probe tip, while the phase change of CN nanosheets is negative, indicating attraction between CN and the probe tip [58]. This once again proves that due to the diffusion motion of carriers, the p region in the p-n junction presents a negative charge, and the n region presents a positive charge, forming an internal electric field directed by CN to Te NPs. When the sample bias increases from 2 V to 5 V, the amplitude of phase change increases (Fig. 4f), confirming the observed results [59]. Under light irradiation, the negative phase of CN and the positive phase of Te NPs tend to become smaller to a certain extent (Fig. 4e–g and Fig. S19), especially at the edge of the sample, where the difference is more obvious than in the dark. This confirmed that photo-induced electrons in the p region migrate to the n region and photo-induced holes in the n region migrate to the p region under the action of the built-in electric field, resulting in the accumulation of photogenerated electrons near the n region and photogenerated

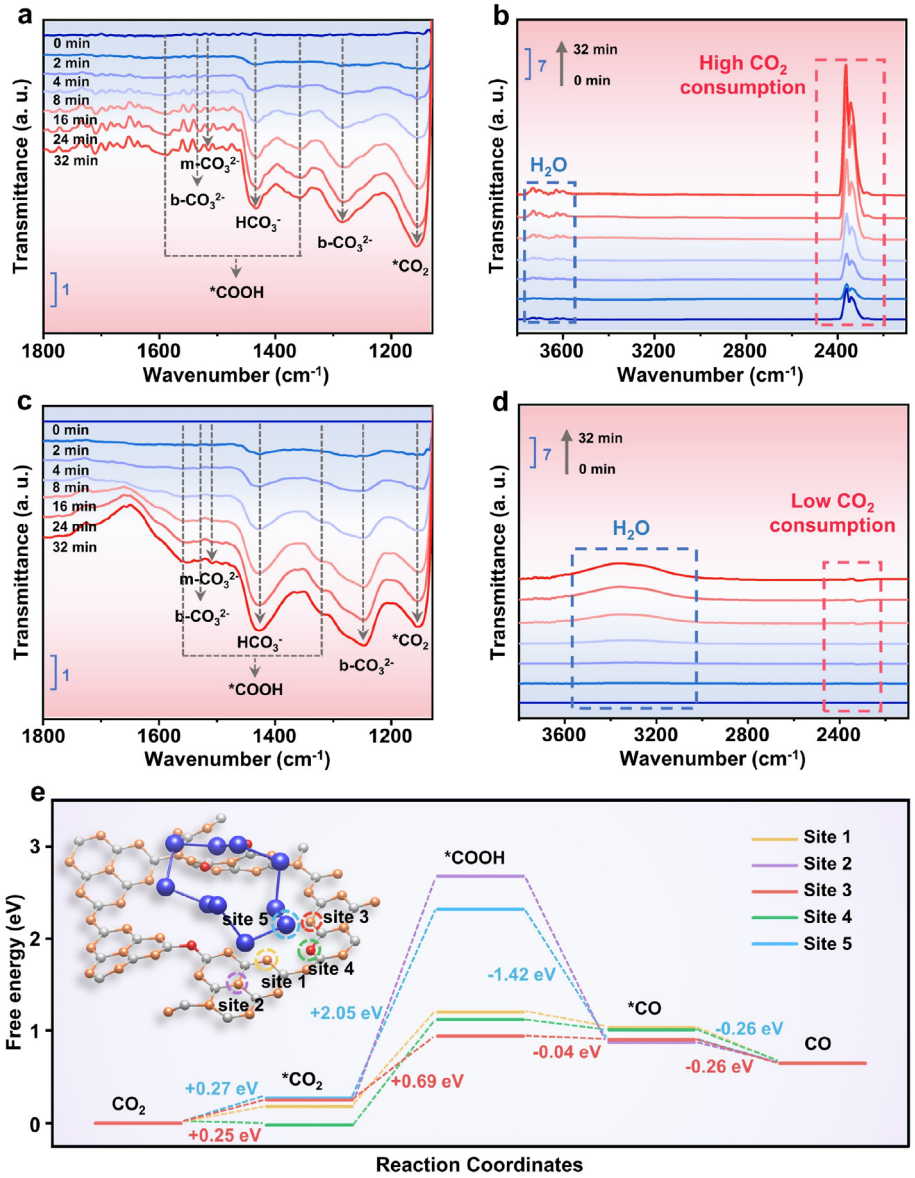

Fig. 5. (a-d) In-situ DRIFTS profiles for illumination processes of Te/CN-NH_3 (a, b) and CN-NH_3 (c, d); (e) Gibbs free energies of CO_2 photoreduction pathways by DFT calculations over possible active sites on the surface of Te/CN-NH_3.

holes near the p region [15].

2.4. Mechanism of photocatalytic reaction

To gain deeper insights into the reaction mechanism, *in-situ* DRITFS was performed to monitor the real-time formation of reaction intermediates during the photocatalytic CO_2 reduction process (Fig. 5a–d). Before light irradiation, the catalyst was revealed to a watery CO_2 gas flowing in the dark for 10 min to saturate the adsorption sites. The consumption and accumulation of different reactive species are represented positive and negative peaks in the infrared spectrogram, respectively. Notably, the peaks observed at 1355 and 1588 cm^{-1} are attributed to the *COOH, a crucial intermediate in the conversion of CO_2 to CO or CH_4 [60], with intensity increasing over irradiation time. Additionally, intermediates such as $*CO_2$ (1150 cm^{-1}), b-CO_3^{2-} (1283 and 1530 cm^{-1}), m-CO_3^{2-} (1514 cm^{-1}) and HCO_3^- (1433 cm^{-1}) were identified [61–63]. And moreover, the peaks of H_2O (about 3600 cm^{-1}) and CO_2 (about 2360 cm^{-1}) are positive [64], illustrating the consumption of H_2O as a proton source and CO_2 as a feedstock in the photoreaction system. Both CN-NH_3 and Te-CN-NH_3 emerged similar infrared absorption patterns of key intermediates in the 1100-2000 cm^{-1} range. Notably, Te-CN-NH_3 displayed a stronger *COOH peak intensity compared to CN-NH_3, indicating that Te-CN-NH_3 is more conducive to the conversion of CO_2 to CO. In addition, Te-CN-NH_3 exhibits higher CO_2 consumption, indicating that Te-CN-NH_3 is conducive to CO_2 photoreduction. These findings show the crucial role of the p-n heterojunction in promoting CO_2 conversion and *COOH production, thereby enhancing the photocatalytic CO_2 reduction performance of Te-CN-NH_3.

DFT calculations were employed to further elucidate the mechanism of CO_2 photoreduction within Te/CN heterojunctions, as well as the improved CO yield and selectivity. The calculated density of states (Fig. S20**)** shows that the 5p orbit of Te matches relatively well with the 2p orbit of N when Te NPs and CN are closely integrated, indicating strong interaction between Te NPs and N on CN [65]. The active site for CO_2 photoreduction on Te/CN-NH_3 was identified through the Gibbs free energy of the reaction (Fig. 5e). The conversion of CO_2* to COOH* emerges as the rate-determining step of CO_2 photoreduction [66]. Within the p-n heterojunction, the bridge nitrogen at CN (site 3) exhibits the lowest energy for COOH* generation, surpassing that of Te NPs (site 5), indicating that the optimal site for CO_2 reduction reaction is at N site of CN. The robust interaction between Te and N on CN facilitates the transfer of photogenerated electrons from Te to N on CN during CO_2 photoreduction, thereby promoting the reduction reaction and increasing CO production. In addition, the adsorption energy of CO at each site within the heterojunction (−0.06 to −0.13 eV) implies a favorable effect on enhancing the selectivity of CO during photocatalytic CO_2RR [67,68].

3. Conclusion

In summary, we engineered a p-n heterojunction by synthesizing ultrasmall Te NPs on CN nanosheets through a tandem hydrothermal-calcination approach, followed by ammonia-assisted calcination. This process yielded Te/CN-NH_3, featuring smaller Te NPs, larger surface area, and increased porosity compared to Te/CN-N_2. Notably, Te/CN-NH_3 exhibited enhanced light absorption and redox capacity for CO_2 reduction and H_2O oxidation. The optimized Te/CN-NH_3 catalyst demonstrated remarkable photocatalytic CO_2 reduction performance, achieving nearly 100% selectivity for CO with a yield of 92.0 μmol g^{-1} h^{-1}, a fourfold increase over pure CN. Furthermore, Te/CN-NH_3 showed superior performance even under low CO_2 concentrations and in air. Various characterization techniques confirmed its robust carrier separation capabilities, corroborated by in-situ KPFM and EFM, which revealed enhanced charge transfer within the heterojunction facilitated by NH_3-assisted calcination strategy. DFT calculations identified the bridge nitrogen at CN as the active site for CO_2 photoreduction on Te/CN-NH_3, with strong Te-N interactions promoting electron transfer during CO_2 reduction. Moreover, in-situ DRITFS indicated Te-CN-NH_3's superior suitability for CO_2 conversion to CO compared to CN-NH_3, highlighting its potential for practical applications. This work contributes valuable insights into designing efficient p-n heterojunction photocatalysts for practical application.

4. Experimental

4.1. Materials

Chemicals: Melamine (99%, Adamas), Telluric acid (98%, Adamas), Tellurium (99%+, 100 mesh, Adamas), Ethanol (99 %+, Greagent).

4.2. Synthesis of Te/CN heterojunction

The 1.0 g of melamine and 0.4 g of telluric acid were added to 50 mL of DI water and dispersed under ultrasonication for 1 h. The obtained homogeneous solution was then transferred to a Teflon-lined stainless-steel autoclave reactor, and was heated at 180 °C for 10 h. Afterward, the reactor was cooled down to room temperature, the resulting solution was subjected to centrifugation twice with DI water and once with ethanol remove impurities, and then dried in an oven at 60 °C. Subsequently, the obtained white powder was loaded into a crucible and put into a tube furnace, and then 5 % NH_3/N_2 gas was passed into the tube furnace, and the temperature was raised to 500 °C for calcination for 4 h at a heating rate of 2.5 °C min^{-1}. Finally, a gray powder was obtained after milling, which was named Te/CN-NH_3. In the same step, the calcination atmosphere was changed to N_2, and the obtained sample was named Te/CN-N_2. The selection of experimental conditions includes the addition amount of telluric acid (including 0.2, 0.3, 0.4, 0.6, 0.8 g) and the calcination temperature (including 450, 480, 500, 520, 550, 580, 600 °C).

4.3. Synthesis of CN nanosheets

Similar to the synthesis procedure of Te/CN heterojunction, except that the precursor did not contain telluric acid, and the samples obtained by calcination in 5% NH_3/N_2 and N_2 atmosphere are pale yellow powder after grinding, which named CN-NH_3 and CN-N_2 respectively.

4.4. Synthesis of Te NPs

The crucible with 1.0 g tellurium powder was placed in a tubular furnace, and calcined at 500 °C for 4 h in 5 % NH_3/N_2 gas at a heating rate of 2.5 °C min^{-1}, and then ground into fine powder.

CRediT authorship contribution statement

Huange Liao: Writing – original draft, Investigation. **Kai Huang:** Writing – original draft, Data curation. **Weidong Hou:** Investigation. **Huazhang Guo:** Investigation. **Cheng Lian:** Investigation. **Jiye Zhang:** Investigation. **Zheng Liu:** Writing – review & editing, Supervision, Funding acquisition. **Liang Wang:** Writing – review & editing, Supervision, Project administration, Funding acquisition.

Declaration of competing interest

The authors declare that they have no known competing financial interests or personal relationships that could have appeared to influence the work reported in this paper.

Acknowledgements

The project was funded by China Postdoctoral Science Foundation (2023T160406) and Shanghai Pujiang Program (21PJD022). This

project was also supported by Singapore Ministry of Education AcRF Tier 2 (MOE-MOET2EP10121-0006) and AcRF Tier 1 (RG7/21). This work is Supported by Shanghai Technical Service Center of Science and Engineering Computing, Shanghai University.

Appendix B. Supplementary data

Supplementary data to this article can be found online at https://doi.org/10.1016/j.apmate.2024.100243.

References

[1] B. Rhimi, M. Zhou, Z. Yan, X. Cai, Z. Jiang, Cu-based materials for enhanced C^{2+} product selectivity in photo-/electro-catalytic CO_2 reduction: challenges and prospects, Nano-Micro Lett. 16 (2024) 64.
[2] J. Tian, J. Li, Y. Guo, Z. Liu, B. Liu, J. Li, Oxygen vacancy mediated bismuth-based photocatalysts, Adv. Powder Mater. 3 (2024) 100201.
[3] H. Charles, R.C. Pawar, H. Khan, C.S. Lee, Photocatalyst engineering for water-based CO_2 reduction under visible light irradiation to enhance CO selectivity: a review of recent advances, Int. J. Pr. Eng. Man. Gt. 10 (2023) 1061–1091.
[4] G.F.S.R. Rocha, M.A.R. da Silva, A. Rogolino, G.A.A. Diab, L.F.G. Noleto, M. Antonietti, I.F. Teixeira, Carbon nitride based materials: more than just a support for single-atom catalysis, Chem. Soc. Rev. 52 (2023) 4878–4932.
[5] J. Ding, Q. Tang, Y. Fu, Y. Zhang, J. Hu, T. Li, Q. Zhong, M. Fan, H.H. Kung, Core–shell covalently linked graphitic carbon nitride–melamine–resorcinol–formaldehyde microsphere polymers for efficient photocatalytic CO_2 reduction to methanol, J. Am. Chem. Soc. 144 (2022) 9576–9585.
[6] L. Chen, M.A. Maigbay, M. Li, X. Qiu, Synthesis and modification strategies of g-C_3N_4 nanosheets for photocatalytic applications, Adv. Powder Mater. 3 (2024) 100150.
[7] Q. Liu, H. Tian, Z. Dai, H. Sun, J. Liu, Z. Ao, S. Wang, C. Han, S. Liu, Nitrogen-doped carbon nanospheres-modified graphitic carbon nitride with outstanding photocatalytic activity, Nano-Micro Lett. 12 (2020) 24.
[8] P. Jiménez-Calvo, Synergy of visible-light responsive photocatalytic materials and device engineering for energy and environment: minireview on hydrogen production and water decontamination, Mater. Today Catalysis 4 (2024) 100040.
[9] J. Fu, J. Yu, C. Jiang, B. Cheng, g-C_3N_4-based heterostructured photocatalysts, Adv. Energy Mater. 8 (2018) 1701503.
[10] Y. Chen, B. Zhang, Y. Liu, J. Chen, H. Pan, W. Sun, Graphitic carbon nitride-based electrocatalysts for energy applications, Mater. Today Catalysis 1 (2023) 100003.
[11] J. Pan, D. Wang, D. Wu, J. Cao, X. Fang, C. Zhao, Z. Zeng, B. Zhang, D. Liu, S. Liu, G. Liu, S. Jiao, Z. Xu, L. Zhao, J. Wang, Rational design of three dimensional hollow heterojunctions for efficient photocatalytic hydrogen evolution applications, Adv. Sci. 11 (2024) 2309293.
[12] L. Sun, Y. Zhuang, Y. Yuan, W. Zhan, X.J. Wang, X. Han, Y. Zhao, Nitrogen-doped carbon-coated CuO-In_2O_3 p–n heterojunction for remarkable photocatalytic hydrogen evolution, Adv. Energy Mater. 9 (2019) 1902839.
[13] B.J. Ng, J.Y. Tang, L.Y. Ow, X.Y. Kong, Y.H. Ng, L.K. Putri, S.P. Chai, Nanoscale p–n junction integration via the synergetic hybridization of facet-controlled Cu_2O and defect-modulated g-C_3N_{4-x} atomic layers for enhanced photocatalytic water splitting, Mater. Today Energy 29 (2022) 101102.
[14] L. Bai, H. Huang, S. Zhang, L. Hao, Z. Zhang, H. Li, L. Sun, L. Guo, H. Huang, Y. Zhang, Photocatalysis-assisted Co_3O_4/g-C_3N_4 p–n junction all-solid-state supercapacitors: a bridge between energy storage and photocatalysis, Adv. Sci. 7 (2020) 2001939.
[15] H. Wang, R. Niu, J. Liu, S. Guo, Y. Yang, Z. Liu, J. Li, Electrostatic self-assembly of 2d/2d $CoWO_4$/g-C_3N_4 p-n heterojunction for improved photocatalytic hydrogen evolution: built-in electric field modulated charge separation and mechanism unveiling, Nano Res. 15 (2022) 6087–6098.
[16] W. He, L. Liu, T. Ma, H. Han, J. Zhu, Y. Liu, Z. Fang, Z. Yang, K. Guo, Controllable morphology $CoFe_2O_4$/g-C_3N_4 p-n heterojunction photocatalysts with built-in electric field enhance photocatalytic performance, Appl. Catal. B Environ. 306 (2022) 101102.
[17] N. Tian, H. Huang, S. Wang, T. Zhang, X. Du, Y. Zhang, Facet-charge-induced coupling dependent interfacial photocharge separation: a case of BiOI/g-C_3N_4 p-n junction, Appl. Catal. B Environ. 267 (2020) 118697.
[18] V. Soni, P. Singh, A.A.P. Khan, A. Singh, A.K. Nadda, C.M. Hussain, Q. Van Le, S. Rizevsky, V.H. Nguyen, P. Raizada, Photocatalytic transition-metal-oxides-based p–n heterojunction materials: synthesis, sustainable energy and environmental applications, and perspectives, J. Nanostruct. Chem. 13 (2023) 129–166.
[19] X. Gong, J. Ye, Y. Wang, S. Su, S. Chen, Y. Xie, Z. Fan, Y. Ling, J. Zhao, Enhancement photoreduction CO_2 performance via constructed C_3N_4/Cu_2O p-n heterojunction, Appl. Catal. A-Gen. 668 (2023) 119489.
[20] Z. Xie, C. Xing, W. Huang, T. Fan, Z. Li, J. Zhao, Y. Xiang, Z. Guo, J. Li, Z. Yang, B. Dong, J. Qu, D. Fan, H. Zhang, Ultrathin 2d nonlayered tellurium nanosheets: facile liquid-phase exfoliation, characterization, and photoresponse with high performance and enhanced stability, Adv. Funct. Mater. 28 (2018) 1705833.
[21] D. Kumaar, M. Can, K. Portner, H. Weigand, O. Yarema, S. Wintersteller, F. Schenk, D. Boskovic, N. Pharizat, R. Meinert, E. Gilshtein, Y. Romanyuk, A. Karvounis, R. Grange, A. Emboras, V. Wood, M. Yarema, Colloidal ternary telluride quantum dots for tunable phase change optics in the visible and near-infrared, ACS Nano 17 (2023) 6985–6997.
[22] K. Wang, D. Liu, L. Liu, X. Li, H. Wu, Z. Sun, M. Li, A.S. Vasenko, S. Ding, F. Wang, C. Xiao, Isolated metalloid tellurium atomic cluster on nitrogen-doped carbon nanosheet for high-capacity rechargeable lithium-CO_2 battery, Adv. Sci. 10 (2023) 2205959.
[23] Y. Yin, P. Xiang, Y. Zhou, H. Meng, X. Xiao, Y. Shao, X. Zhang, J. Zhou, Q. Li, C. Guo, X. Ma, L. Zhang, L. Zhang, Q. Zhang, B. Jiang, Creation of interfacial S_4-Sn-N_2 electron pathways for efficient light-driven hydrogen evolution, Small 20 (2024) 2310664.
[24] N. Meng, J. Ren, Y. Liu, Y. Huang, T. Petit, B. Zhang, Engineering oxygen-containing and amino groups into two-dimensional atomically-thin porous polymeric carbon nitrogen for enhanced photocatalytic hydrogen production, Energy Environ. Sci. 11 (2018) 566–571.
[25] W. Hou, H. Xu, Y. Cai, Z. Zou, D. Li, D. Xia, Precisely control interface ovs concentration for enhance 0d/2d $Bi_2O_2CO_3$/BiOCl photocatalytic performance, Appl. Surf. Sci. 530 (2020) 147218.
[26] Y. Zeng, C. Li, B. Li, J. Liang, M.J. Zachman, D.A. Cullen, R.P. Hermann, E.E. Alp, B. Lavina, S. Karakalos, M. Lucero, B. Zhang, M. Wang, Z. Feng, G. Wang, J. Xie, D.J. Myers, J.P. Dodelet, G. Wu, Tuning the thermal activation atmosphere breaks the activity–stability trade-off of Fe–N–C oxygen reduction fuel cell catalysts, Nat. Catal. 6 (2023) 1215–1227.
[27] C. Cheng, L. Mao, X. Kang, C.L. Dong, Y.C. Huang, S. Shen, J. Shi, L. Guo, A high-cyano groups-content amorphous-crystalline carbon nitride isotype heterojunction photocatalyst for high-quantum-yield H_2 production and enhanced CO_2 reduction, Appl. Catal. B Environ. 331 (2023) 122733.
[28] C. Ma, J. Yan, Y. Huang, C. Wang, G. Yang, The optical duality of tellurium nanoparticles for broadband solar energy harvesting and efficient photothermal conversion, Sci. Adv. 4 (2018) eaas9894.
[29] F. Chen, L.L. Liu, J.H. Wu, X.H. Rui, J.J. Chen, Y. Yu, Single-atom iron anchored tubular g-C_3N_4 catalysts for ultrafast fenton-like reaction: roles of high-valency iron-oxo species and organic radicals, Adv. Mater. 34 (2022) 2202891.
[30] K. Li, C. Liu, J. Li, G. Wang, K. Wang, Architecting inorganic/organic S-scheme heterojunction of $Bi_4Ti_3O_{12}$ coupling with g-C_3N_4 for photocatalytic H_2O_2 production from pure water, Acta Phys. Chim. Sin. 40 (2024) 2403009.
[31] B. Qu, P. Li, L. Bai, Y. Qu, Z. Li, Z. Zhang, B. Zheng, J. Sun, L. Jing, Atomically dispersed Zn-N_5 sites immobilized on g-C_3N_4 nanosheets for ultrasensitive selective detection of phenanthrene by dual ratiometric fluorescence, Adv. Mater. 35 (2023) 2211575.
[32] Z. Wang, G. Li, W. Hou, H. Guo, L. Wang, M. Wu, Insights into the use of Te–O pairs as active centers of carbon nanosheets for efficient electrochemical oxygen reduction, ACS Nano 17 (2023) 8671–8679.
[33] Y. Zhang, W. Lu, P. Zhao, M.H. Aboonasr Shiraz, D. Manaig, D.J. Freschi, Y. Liu, J. Liu, A durable lithium–tellurium battery: effects of carbon pore structure and tellurium content, Carbon 173 (2021) 11–21.
[34] B. Hu, K. Huang, B. Tang, Z. Lei, Z. Wang, H. Guo, C. Lian, Z. Liu, L. Wang, Graphene quantum dot-mediated atom-layer semiconductor electrocatalyst for hydrogen evolution, Nano-Micro Lett. 15 (2023) 217.
[35] G. Zhao, B. Li, X. Yang, X. Zhang, Z. Li, D. Jiang, H. Du, C. Zhu, H. Li, C. Xue, Y. Yuan, Two birds with one stone: engineering polymeric carbon nitride with n-π^* electronic transition for extending light absorption and reducing charge recombination, Adv. Powder Mater. 2 (2023) 100077.
[36] J. Liang, W. Zhang, Z. Liu, Q. Song, Z. Zhu, Z. Guan, H. Wang, P. Zhang, J. Li, M. Zhou, C. Cao, H. Xu, Y. Lu, X. Meng, L. Song, P.K. Wong, Z. Jiang, C.S. Lee, Tuning metal-free hierarchical boron nitride-like catalyst for enhanced photocatalytic CO_2 reduction activity, ACS Catal. 12 (2022) 12217–12226.
[37] K. Talbi, F. Penas-Hidalgo, A.L. Robinson, P. Gotico, W. Leibl, P. Mialane, M. Gomez-Mingot, M. Fontecave, A. Solé-Daura, C. Mellot-Draznieks, A. Dolbecq, Photocatalytic CO_2 reduction by Ni-substituted polyoxometalates: structure-activity relationships and mechanistic insights, Appl. Catal. B Environ. Energy 345 (2024) 123681.
[38] K. Wang, H. Qin, J. Li, Q. Cheng, Y. Zhu, H. Hu, J. Peng, S. Chen, G. Wang, S. Chou, S. Dou, Y. Xiao, Metallic $AgInS_2$ nanocrystals with sulfur vacancies boost atmospheric CO_2 photoreduction under near-infrared light illumination, Appl. Catal. B Environ. 332 (2023) 122763.
[39] Y. Ma, Y. Zhang, G. Xie, Z. Huang, L. Peng, C. Yu, X. Xie, S. Qu, N. Zhang, Isolated Cu sites in CdS hollow nanocubes with doping-location-dependent performance for photocatalytic CO_2 reduction, ACS Catal. 14 (2024) 1468–1479.
[40] W. Lyu, Y. Liu, J. Zhou, D. Chen, X. Zhao, R. Fang, F. Wang, Y. Li, Modulating the reaction configuration by breaking the structural symmetry of active sites for efficient photocatalytic reduction of low-concentration CO_2, Angew. Chem. Int. Ed. 62 (2023) e202310733.
[41] L. Xie, C. Liang, Y. Wu, K. Wang, W. Hou, H. Guo, Z. Wang, Y.M. Lam, Z. Liu, L. Wang, Isomerization engineering of oxygen-enriched carbon quantum dots for efficient electrochemical hydrogen peroxide production, Small 20 (2024) 2401253.
[42] K. Li, J. Mei, J. Li, Y. Liu, G. Wang, D. Hu, S. Yan, K. Wang, Boosting the photosynthesis of hydrogen peroxide directly from pure water and air over S-scheme fiber heterojunction, Sci. China Mater. 67 (2024) 484–492.
[43] C. Liao, W. Jing, F. Wang, Y. Liu, 3D In_2S_3/C/Fe_3C nanofibers for Z-scheme photocatalytic CO_2 conversion to acetate, Mater. Today Catalysis 3 (2023) 100030.
[44] X. Shao, K. Li, J. Li, Q. Cheng, G. Wang, K. Wang, Investigating S-scheme charge transfer pathways in NiS@Ta_2O_5 hybrid nanofibers for photocatalytic CO_2 conversion, Chin. J. Catal. 51 (2023) 193–203.
[45] R.C. Pawar, P.J. Chengula, H. Khan, H. Charles, C.S. Lee, Boosting photocatalytic CO_2 conversion using strongly bonded Cu/reduced Nb_2O_5 nanosheets, Dalton Trans. 52 (2023) 12832–12844.

[46] H. Guo, L. Zhou, K. Huang, Y. Li, W. Hou, H. Liao, C. Lian, S. Yang, D. Wu, Z. Lei, Z. Liu, L. Wang, Nitrogen-rich carbon dot-mediated n→π* electronic transition in carbon nitride for superior photocatalytic hydrogen peroxide production, Adv. Funct. Mater. 34 (2024) 2402650.
[47] H. Guo, Y. Lu, Z. Lei, H. Bao, M. Zhang, Z. Wang, C. Guan, B. Tang, Z. Liu, L. Wang, Machine learning-guided realization of full-color high-quantum-yield carbon quantum dots, Nat. Commun. 15 (2024) 4843.
[48] Q. Ren, Y. He, H. Wang, Y. Sun, F. Dong, Photo-switchable oxygen vacancy as the dynamic active site in the photocatalytic NO oxidation reaction, ACS Catal. 12 (2022) 14015–14025.
[49] J. Zheng, Z. Lei, Incorporation of CoO nanoparticles in 3d marigold flower-like hierarchical architecture $MnCo_2O_4$ for highly boosting solar light photo-oxidation and reduction ability, Appl. Catal. B Environ. 237 (2018) 1–8.
[50] Y. Wang, E. Chen, J. Tang, Insight on reaction pathways of photocatalytic CO_2 conversion, ACS Catal. 12 (2022) 7300–7316.
[51] D. Zhao, Y. Wang, C.L. Dong, Y.C. Huang, J. Chen, F. Xue, S. Shen, L. Guo, Boron-doped nitrogen-deficient carbon nitride-based Z-scheme heterostructures for photocatalytic overall water splitting, Nat. Energy 6 (2021) 388–397.
[52] D. Chen, R. Lu, R. Yu, Y. Dai, H. Zhao, D. Wu, P. Wang, J. Zhu, Z. Pu, L. Chen, J. Yu, S. Mu, Work-function-induced interfacial built-in electric fields in Os-$OsSe_2$ heterostructures for active acidic and alkaline hydrogen evolution, Angew. Chem. Int. Ed. 61 (2022) e202208642.
[53] F. Liu, R. Shi, Z. Wang, Y. Weng, C.M. Che, Y. Chen, Direct Z-scheme hetero-phase junction of black/red phosphorus for photocatalytic water splitting, Angew. Chem. Int. Ed. 58 (2019) 11791–11795.
[54] K. Wang, Q. Cheng, W. Hou, H. Guo, X. Wu, J. Wang, J. Li, Z. Liu, L. Wang, Unlocking the charge-migration mechanism in S-scheme junction for photoreduction of diluted CO_2 with high selectivity, Adv. Funct. Mater. 34 (2023) 2309603.
[55] B. Huang, X. Fu, K. Wang, L. Wang, H. Zhang, Z. Liu, B. Liu, J. Li, Chemically bonded $BiVO_4$/$Bi_{19}Cl_3S_{27}$ heterojunction with fast hole extraction dynamics for continuous CO_2 photoreduction, Adv. Powder Mater. 3 (2024) 100140.
[56] J. Jing, J. Yang, W. Li, Z. Wu, Y. Zhu, Construction of interfacial electric field via dual-porphyrin heterostructure boosting photocatalytic hydrogen evolution, Adv. Mater. 34 (2022) 2106807.
[57] T. Kanata-Kito, M. Matsunaga, H. Takakura, Y. Hamakawa, T. Nishino, Photoreflectance characterization of built-in potential in mbe-produced as-grown gaas surface, Proc. SPIE 1286 (1990) 56–65.
[58] R. Zhuravel, A. Stern, N. Fardian-Melamed, G. Eidelshtein, L. Katrivas, D. Rotem, A.B. Kotlyar, D. Porath, Advances in synthesis and measurement of charge transport in DNA-based derivatives, Adv. Mater. 30 (2018) 1706984.
[59] P. Zhao, N. Soin, K. Prashanthi, J. Chen, S. Dong, E. Zhou, Z. Zhu, A.A. Narasimulu, C.D. Montemagno, L. Yu, J. Luo, Emulsion electrospinning of polytetrafluoroethylene (PTFE) nanofibrous membranes for high performance, ACS Appl. Mater. Interfaces 10 (2018) 5880–5891.
[60] X. Li, L. Li, G. Chen, X. Chu, X. Liu, C. Naisa, D. Pohl, M. Löffler, X. Feng, Accessing parity-forbidden d-d transitions for photocatalytic CO_2 reduction driven by infrared light, Nat. Commun. 14 (2023) 4034.
[61] Y. Yang, Z. Chai, X. Qin, Z. Zhang, A. Muhetaer, C. Wang, H. Huang, C. Yang, D. Ma, Q. Li, D. Xu, Light-induced redox looping of a rhodium/Ce_xWO_3 photocatalyst for highly active and robust dry reforming of methane, Angew. Chem. Int. Ed. 61 (2022) e202200567.
[62] S. Bai, W. Jing, G. He, C. Liao, F. Wang, Y. Liu, L. Guo, Near-infrared-responsive photocatalytic CO_2 conversion via in situ generated Co_3O_4/Cu_2O, ACS Nano 17 (2023) 10976–10986.
[63] J.P. Dong, Y. Xu, X.G. Zhang, H. Zhang, L. Yao, R. Wang, S.Q. Zang, Copper-sulfur-nitrogen cluster providing a local proton for efficient carbon dioxide photoreduction, Angew. Chem. Int. Ed. 62 (2023) e202313648.
[64] Y. Liu, J. Sun, H. Huang, L. Bai, X. Zhao, B. Qu, L. Xiong, F. Bai, J. Tang, L. Jing, Improving CO_2 photoconversion with ionic liquid and Co single atoms, Nat. Commun. 14 (2023) 1457.
[65] J.J. Yang, Y. Zhang, X.Y. Xie, W.H. Fang, G. Cui, Photocatalytic reduction of carbon dioxide to methane at the Pd-supported TiO_2 interface: mechanistic insights from theoretical studies, ACS Catal. 12 (2022) 8558–8571.
[66] Y. Xu, W. Hou, K. Huang, H. Guo, Z. Wang, C. Lian, J. Zhang, D. Wu, Z. Lei, Z. Liu, L. Wang, Engineering built-in electric field microenvironment of CQDs/g-C_3N_4 heterojunction for efficient photocatalytic CO_2 reduction, Adv. Sci. 11 (2024) 2403607.
[67] P. Chen, B. Lei, X.a. Dong, H. Wang, J. Sheng, W. Cui, J. Li, Y. Sun, Z. Wang, F. Dong, Rare-earth single-atom La–N charge-transfer bridge on carbon nitride for highly efficient and selective photocatalytic CO_2 reduction, ACS Nano 14 (2020) 15841–15852.
[68] H. Guo, J. Raj, Z. Wang, T. Zhang, K. Wang, L. Lin, W. Hou, J. Zhang, M. Wu, J. Wu, L. Wang, Synergistic effects of amine functional groups and enriched-atomic-iron sites in carbon dots for industrial-current–density CO_2 electroreduction, Small 20 (2024) 2311132.

Huange Liao is pursuing her master degree in Chemical Engineering and Technology supervised by Prof. Liang Wang at School of Environmental and Chemical Engineering, Shanghai University. Her research focuses on the mechanisms of nanocatalytic materials used in photocatalytic CO_2 conversion.

Prof. Wang Liang received his Ph.D. degree from the School of Environmental and Chemical Engineering at Shanghai University in 2012, and completed his post-doctoral research at Shanghai University in 2014. From 2018 to 2019, he was a visiting scholar at Rice University, United States. In 2021, he was promoted to a professor of Shanghai University. From 2022 to 2023, he worked as a visiting research fellow at Nanyang Technological University (NTU), Singapore. His research focuses on the green and controllable preparation and application of carbon functional nanomaterials. In recent years, he has published over 100 SCI papers, including 18 ESI highly cited papers with over 8500 citations and an H-index of 50. He has been recognized as one of the top 2 % of scientists in the world four times and has been awarded the title of Shanghai Eastern Scholar.

Prof. Zheng Liu received his Ph.D at National Center for Nanoscience and Technology (NCNST, China), working on the synthesis and energy harvest of carbon nanotubes. He is currently the President's Chair Professor at NTU and Materials Research Society of Singapore Chair Professorship. He has published over 350 papers, including over 60 ESI highly cited papers with over citations 60000 and an H-index of 123, and has been selected as a Clarivate Analytics Global Highly Cited Researcher for five consecutive years. His awards include the APEC Science Innovation, Research and Education Award (ASPIRE Award), Singapore Young Scientist Award, ICON-2DMAT Young Scientists, Asia's Rising Scientists, the Nanyang Research Award and more.